Journal Name

Dynamic Article Links►

Cite this: DOI: 10.1039/c0xx00000x

www.rsc.org/xxxxxx

ARTICLE TYPE

Impacts of ionic liquid capping on morphology and photocatalytic performance of $SbPO_4$ crystals

ShunqiangChen,[a]Yutong Di,[a]Taohai Li*[a] , Feng Li[a] and Wei Cao[b]

Received (in XXX, XXX) Xth XXXXXXXXX 20XX, Accepted Xth XXXXXXXXX 20XX

DOI: 10.1039/b000000x

By using [BMIM][PO_4] as a coupling agent, a novel hydrothermal method is developed to prepare microspherical $SbPO_4$ with different morphologies and photocatalytic abilities. An evolution from flower- to sphere-shaped products was observed. Regular $SbPO_4$ microspheres with diameters of 10-35 μm were found to exhibit excellent photocatalytic properties to degrade the rhodamine B (45 min, 99 %) and methylene blue (60 min, 99 %) under UV light irradiation. Impacts of the ionic liquid type, capping abilities and reaction conditions on final products were revealed. It is found that by tuning reaction time and temperature, the [BMIM][PO4] can gradually react with $SbCl_3$, forming the $SbPO_4$ products with controllable morphology of and tailored bandgap. Distinguished photocatalytic abilities are attributed to large surface area and low bandgap energy of the semiconductor.

Introduction

Photocatalytic degradation of toxic organic pollutants has drawn great interests due to its environmentally friendly merits.[1-3] To date, photocatalysts are emphasized on semiconductor materials thanks to their promising photodegrade ability of organic contaminants[4] and solar energy conversion.[5] These semiconductor materials can be endowed with narrow bandgap, large surface area, specific morphology and structure through proper synthetic routes, such as the hydrothermal method.[6,7] Conventionally, photocatalytic materials are limited within semiconductors containing TiO_2,[8] In_2O_3,[9] and ZrO_2,[10] etc. Recent researches showed that other chemical composites containing Bi_2O_3,[11] SnO_2,[12] and Sb_2S_3,[13]are also functional as active sites for photocatalysis.[14] Among them, the antimony-based materials have been extensively investigated because of their excellent optical properties[15] and potential applications in sunlight harvesting.[16] Numerous efforts were elaborated in studies of the Sb-based photocatalysts, such as Sb_2S_3,[16] Sb_2WO_6,[17] Sb_2O_3,[18] and $M_2Sb_2O_7$ (M = Ca, Sr),[14] etc. The $SbPO_4$ microsphere with 4.42 eV of band gap energy is a new promising photocatalyst under UV light irradiation.[19] Despite of a few reports on its preparation through hydrothermal reaction[19] and solvothermal decomposition method,[20] improvements of material's synthesis routes and photocatalytic functionality are scarcely reported.

Besides electronic structures, photocatalytic ability of the semiconductors also depends on materials size, morphology, surface area and structure. In this regard, the hydrothermal synthesis is advantageous in controlling these extrinsic properties[21], benefitting the final photocatalytic performances of the $SbPO_4$. Proper media and conditions are essential during the wet synthesis.[6] It is noticed that the ionic liquids (ILs) are widely employed as the reagents in other compound preparations due to their remarkable thermal and chemical stability, dissolving ability, high ionic conductivity and low potentiallytoxicity.[22,23] As a capping agent and phosphorus source, the 1-butyl-3-methylimidazolium phosphate ([BMIM]P) ionic liquid plays an important role in the facile and efficient synthesis of the $SbPO_4$.[24] Inspired by these progresses, the hydrothermal synthesis of $SbPO_4$ is naturally extended to use the [BMIM][PO_4] as a new phosphors source, and vary reaction parameters to tailor product properties.

In this paper, we report on a facile hydrothermal method to prepare $SbPO_4$ with the [BMIM][PO4] as a coupling agent, and study its impact on the morphology and catalytic ability of the final products. The morphological evolution of the products is studied. The photocatalytic ability was evaluated by degrading rhodamine B (RhB) and methylene blue (MB) under UV light irradiation. It is found that the homogeneous $SbPO_4$ microspheres can eliminate these dyes within an hour timespan.

Experimental Section

Materials

Reagents of the 1-butyl-3-methylimidazolium phosphate ([BMIM][PO_4]), $SbCl_3$, $Na_2HPO_4{\cdot}12H_2O$, RhB, MB were of analytical grade and used without further purification. All the chemicals in our experiments were purchased from Shanghai Chemical Reagents Company (China).

Catalysts preparation.

In a typical process, 2 mmol of [BMIM][PO_4] was added in 15 mL water and continuously stirred for 10 min at room temperature until a homogeneous solution was obtained. Then, 2 mmol of $SbCl_3$ was quickly added into the beaker. The mixture was magnetically stirred for 30 minutes. It was transferred into a Teflon-lined autoclave, kept at 160℃ for 24 h and cooled down to room temperature naturally. The resulted white-colored precipitate was separated by centrifugation, washed with deionized water and absolute ethanol 3 times, respectively. It was transferred to an oven and dried at 70℃ for 12 h. The collected product was named as S-P-2.

To study morphology impacts on photocatalytic reactivity, other $SbPO_4$ samples were also fabricated by varying reaction temperature (S-P-1, S-P-3), Sb/P mole ratios (S-M-1, S-M-2) and reaction time (S-T-1, S-T-2). The detailed reaction parameters were tabulated in Table 1. The $SbPO_4$ with other organic phosphate salt (1-ethyl-3-methylimidazolium methyl phosphate) and the $SbPO_4$ without ILs were also prepared in the same procedure. The obtained sample was designated as S-O-1, S-O-2, S-O-3 and S-P-4.

Table 1. Experimental parameters for the synthesis of $SbPO_4$

Sample	Reactants		Temperature (℃)	Time (h)
S-P-1	2 mmol of [BMIM][PO_4] ,	2 mmol of $SbCl_3$	140	24
S-P-2	2 mmol of [BMIM][PO_4],	2 mmol of $SbCl_3$	160	24
S-P-3	2 mmol of [BMIM][PO_4],	2 mmol of $SbCl_3$	180	24
S-P-4	2 mmol of $Na_2HPO_4 \cdot 12H_2O$,	2 mmol of $SbCl_3$	160	24
S-M-1	1 mmol of [BMIM][PO_4],	2 mmol of $SbCl_3$	160	24
S-M-2	3 mmol of [BMIM][PO_4],	2 mmol of $SbCl_3$	160	24
S-T-1	2 mmol of [BMIM][PO_4],	2 mmol of $SbCl_3$	160	12
S-T-2	2 mmol of [BMIM][PO_4],	2 mmol of $SbCl_3$	160	48
S-O-1	2 mmol of [EMIM]DMP,	2 mmol of $SbCl_3$	160	12
S-O-2	2 mmol of [EMIM]DMP,	2 mmol of $SbCl_3$	160	24
S-O-3	2 mmol of [EMIM]DMP,	2 mmol of $SbCl_3$	160	48

Characterization

The crystal structure of the $SbPO_4$ was studied through the X-ray diffraction (XRD) patterns on an X-ray diffractometer (XRD, D/max-RB, Rigaku, Japan) with the Cu-Kα radiation (λ=0.15418 nm) as the incident source. The surface morphology was recorded through the scanning electron microscopy (SEM, JSM-6700F, JEOL, Japan), while grain sizes were obtained via the transmission electron microscopy (TEM, JEM-2100F, JEOL, Japan). The Brunauer-Emmett-Teller (BET) surface area was examined on an ASAP 2010 Brunauer−Emmett−Teller (BET) analyzer. Element compositions were determined through the energy dispersive X-ray spectroscopy (EDX, EX-250, Horiba, Japan). Chemical states of elements were studied via X-ray photoelectron spectroscopy carried out through the XPS Escalab 250, Thermo Scientific, USA. Bandgaps the products were deduced from UV-vis spectra which were performed on a UV–vis spectrophotometer (Lambda 950, Perkin-Elmer, USA). The photoluminescence (PL) spectra were measured on a HitachiF-7000 spectrophotometer with the excitation wavelength of 220 nm.

Measurements of photocatalytic activity

The photocatalytic abilities were determined by the RhB and MB degradation. A 500 W UV-C lamp was used as the light source and placed 8 cm from the reactor. With vigorous stirring, 50 mL of RhB (or MB) (10 mg/L) aqueous solution was mixed with 0.05 gas-prepared photocatalysts. Prior to photoreaction, the solution was stirred in dark for about 30 min to reach the RhB (or MB) adsorption-desorption equilibrium. At regular intervals, 3 mL samples were taken and filtered to remove the particles. The concentration of RhB (or MB) was determined by monitoring peaks of RhB at 552 nm (or MB at 664 nm) measured by a UV-Vis spectrophotometer (Lambda 950, Perkin-Elmer, USA).

Results and discussion

X-ray diffraction.

Figure 1 shows the XRD patterns of $SbPO_4$ (S-P-1, S-P-2, S-P-3) prepared with the assistance of the [BMIM][PO_4] IL, and the one without IL (S-P-4). Sharp characteristic peaks locate at the 2θ angles of 21.8°, 22.9°, 24.6°, 26.3°, 26.7°, 29.8°, 35.2°, 36.3°, 37.8°, 43.8° and 54.3°. They are well indexed to the monoclinic $SbPO_4$ (JCPDS Card NO. 35-0829, space group P21/m, unit-cell parameters a=5.106 (2) Å, b=6.772 (1) Å, c=5.092 (2) Å), denoting that these products are monoclinic structure with high degree of crystallinity.

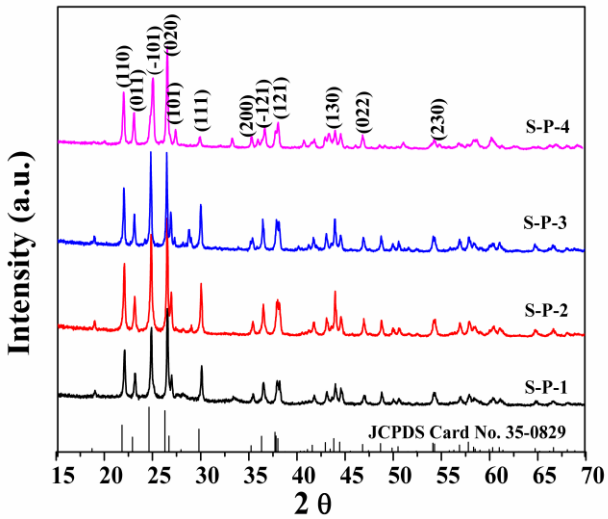

Figure 1. XRD patterns of $SbPO_4$ samples prepared at different hydrothermal parameters.

The XRD patterns of $SbPO_4$ prepared at different Sb/P mole ratio and hydrothermal time are shown in Figure S1, S2 at the Electronic Supplementary Information (ESI). Some additional diffraction peaks with 2θ at 33.1°and 29.2°are observed, which are indexed to the $Sb(PO_4)_3$(JCPDS Card NO. 51-0234)and $SbOPO_4$(JCPDS Card NO. 40-0037).

SEM and HRTEM analysis.

Figure 2 shows the SEM images of the as-prepared samples. From the figure, the diameter of the microspheres was found around 10-35 um. At the beginning of forming stage (S-P-1, Figure 2a) the sample was flower-like $SbPO_4$ microspheres with diameters of 32–38 μm. The well-dispersed product was composed of primary nanorods and nanoplates as observed on the rough surface. With the increase of the reaction temperature, the diameters of the flower-like microspheres decrease to 28-33 μm. As shown in Fig. 2c, the surfaces of these flower-like microspheres are smoother than that of S-P-1. When After adjusting synthesis temperature to 180 ℃ (S-P-3, Figure 2c) the microflowers evolved to sphere-like $SbPO_4$ with partially broken and shriveled debris. It can be seen clearly from Figure 2d that compared to the flower-like microspheres (Figure 2a, b, c), increasing the temperature of the reaction would result in the decrease of product's diameter. Furthermore, the morphologies and surface roughness have obvious changes compared with microflowers. The initial flower-like structure formed by nanorods and nanoplates exhibits a high porosity, and eventually turned into a compacted sphere-like structure with a smooth surface. Compared to the ionic-liquid-assisted $SbPO_4$, the non-ionic-liquid-assisted $SbPO_4$ shown in Figure 2d are rather consisted of nanorods and nanoplates.

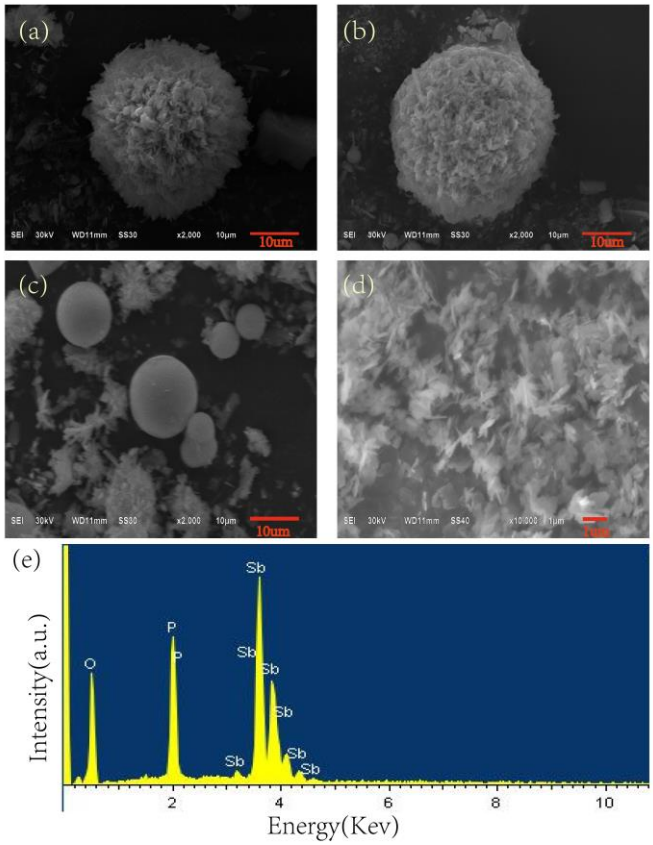

Figure 2. SEM images of the $SbPO_4$ synthesized at different temperatures: (a) S-P-1, (b) S-P-2, (c) S-P-3, (d) S-P-4,

(e) EDX spectrum of S-P-2.

Indeed, similar morphological transformations were observed in other synthetic crystal systems.[19, 25] Moreover, the change of the Sb/P mole ratio can also result in similar evolution (see Fig. S3 in ESI). The EDX analysis of S-P-2 (Figure 2e) confirms the elements of Sb, P and O at a ratio of 1:1:4, very near to the stoichiometric value.

Figure 3 shows high-magnification SEM, the TEM, high resolution TEM (HRTEM) images and selected area electron diffraction (SAED) patterns of S-P-2. The TEM images with more detailed information (Figure 3a, b) reveal that the S-P-2 was composed of nanorods and nanoplates, in consistent with the SEM results. As shown in Figure 3c, the HRTEM image of the microsphere clearly identify the lattice spacing of $SbPO_4$, which matches well with the XRD analyses. The 0.17 nm d-spacing is corresponding to the (111) crystal plane of $SbPO_4$ microspheres. The SAED pattern (Figure 3d) of S-P-2 microspheres clearly confirms that the microsphere is only consisted of the monoclinic $SbPO_4$.

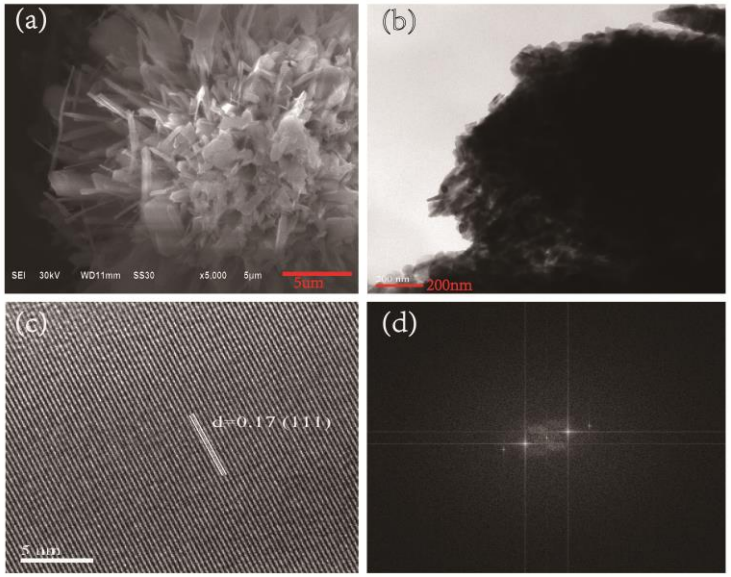

Figure 3. (a) high-magnification SEM images of S-P-2 (b) TEM images of S-P-2, (c) HRTEM image of S-P-2, (d) SAED pattern of S-P-2.

Growth mechanism of $SbPO_4$microspheres.

We first exam the influences of preparation time on the morphology of the final product. A series of preparations was performed by varying the hydrothermal time and keeping other conditions unchanged. First, the XRD characterization is used to study the phase evolution process and depicted in Fig. S11. The product is amorphous at a short reaction time of 4h. It turns to pure $Sb_8O_{11}Cl_2$ (JCPDS no.21-0052) when the reaction time reaches 8h. Moreover, the intensity of the characteristic peak (2θ = 27.94°) of the $Sb_8O_{11}Cl_2$ phase gradually decrease while the one from $SbPO_4$ increase with the reaction time. Pure $SbPO_4$ was generated after 12h of hydrothermal treatment. This shows that the original product $Sb_8O_{11}Cl_2$ has gradually transformed into $SbPO_4$ during the IL-assisted preparation.

Morphological evolution was also studied. The SEM images of the products are shown in Figure 4, where differences in morphologies bear the $SbPO_4$ formation stages. Generally, the microspheres assembly process has been observed for the formation of the $SbPO_4$ microspheres.[25, 26]The 2D nanoplates were formed in the early stages of synthesis, and stick to each other (Figure 4a). Later, the 2D nanorods and nanoplates will grow to 3D microspheres with obviously concaves at the spherical centres of the samples (Figure 4b). The surface roughness of the as-prepared samples decreases with reaction time (12 h, 24 h, Figure 4c, d). Based on the above evidences, a probable formation mechanism of the $SbPO_4$ microspheres was concluded in the Scheme 1.

In order to investigate the influence of ILs on the controllable fabrication and morphology of the obtained $SbPO_4$, another organic phosphate salt ([EMIM]DMP) was used as the reagent instead of the [BMIM][PO_4]. Figure S5 explicitly shows that as-synthesized S-O-1, S-O-2 and S-O-3 with different hydrothermal reaction time are microrods with widths of 4.55-6.13μm and length of 15.29-23.04μm. Morphologies are influenced by the species of ILs.

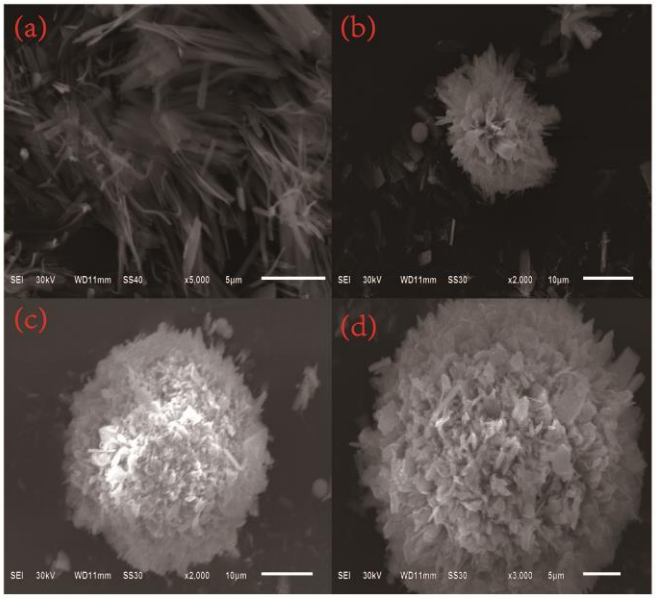

Figure 4. SEM images of the $SbPO_4$ fabricated at different reaction time: (a) 4, (b) 8, (c)12, (d)24.

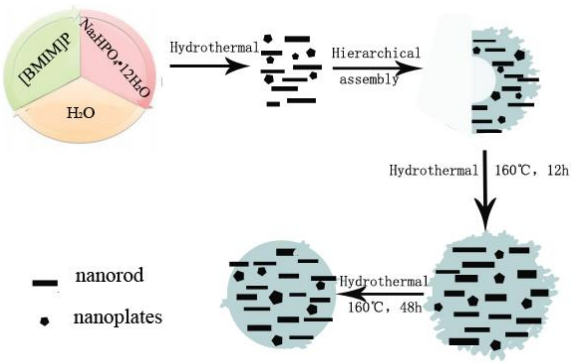

Scheme 1. The schematic illustration of the formation of $SbPO_4$solid microspheres.

XPS analysis

The elemental compositions and chemical states of S-P-2 were further measured by the XPS and the detailed results are displayed in Figure 5. The spectral energies were calibrated by using the adventitious C 1s peak at 284.8 eV. The XPS of the Sb $3d_{3/2}$ is depicted in Figure 5a, P 2p in Figure 5b, and the O 1s in Figure 5c. A binding energy of 540.40 eV is assigned to the $3d_{3/2}$ from the Sb^{3+} ions.[27] Peaking at 133.76 eV, the phosphorus 2p spectrum denotes the element is in the form of P^{5+}.[3] Figure 5c demonstrates that the single peak of O 1s is centered at 531.17 eV.[28] Chemical states of the elements confirm the $SbPO_4$ is the final product.

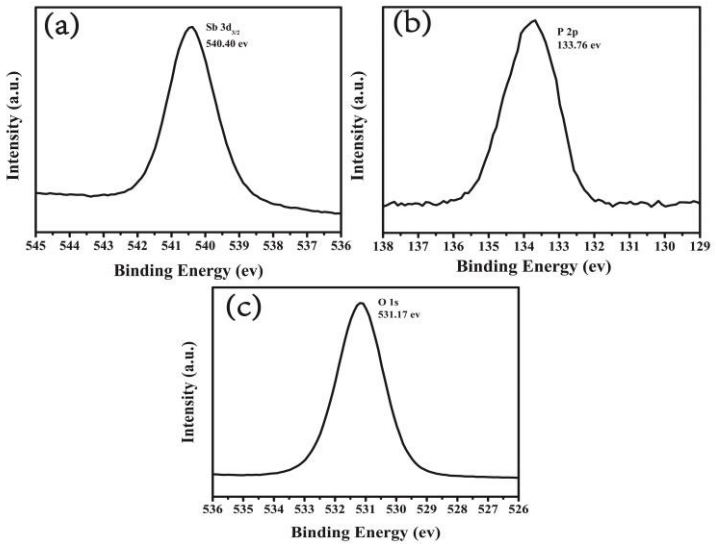

Figure 5. XPS spectra of S-P-2: (a) Sb 3d3/2 peak, (b) P 2p peak, (c) O 1s peak

Optical properties

The bandgaps of the products were determined from UV-Vis diffuse reflection spectra, as shown in Fig.6 for S-P-1, S-P-2, S-P-3, S-P-4 and ILs. The curves exhibit a clear absorption edge of S-P-4 at about 283 nm, in consistence with the previous results.[19] However, the absorbance of S-P-1, S-P-2 and S-P-3 (Figure 6a) is obviously enhanced at the range of 300–600 nm but not at 650-700 nm originated from the IL absorption (Figure S10). Thus, the substantial red shift in the bandgap transition of the ionic-liquid-assisted $SbPO_4$ is attributed to the changes in morphology of the $SbPO_4$ samples. Compared with S-P-3 prepared at 180℃, S-P-1 and S-P-2 also show red shifts in the bandgap transitions. This is most probably attributed to the relatively defective surface as shown in Fig.2. Such redshifts may also be beneficial to enable the utilization of UV-light for the photocatalytic degradation of the dyes.[29]

The bandgap energy (Eg) of the sample follows the equation:

$\alpha=A((h\upsilon-Eg)^{n/2})/(h\upsilon)$

where α, υ, A, and Eg are absorption coefficient, light frequency, a constant and band gap energy (eV), respectively. Among them, the value of n depends on whether the transition is direct (n = 1) or indirect (n = 4).[30] The bandgap energies obtained from plots $(absorbance)^2$ versus energy $(h\upsilon)^2$ (Figure 6b) are about 3.19, 2.80, 4.12 and 4.71 eV for S-P-1, S-P-2, S-P-3 and S-P-4, respectively. A relatively low bandgap of 2.80 eV was found for the S-P-2. It is mention worth that the adsorption band of [BMIM][PO_4] ion pair is around 550nm (Figure S10)[31], out of the regions of samples' bandgap distributions.

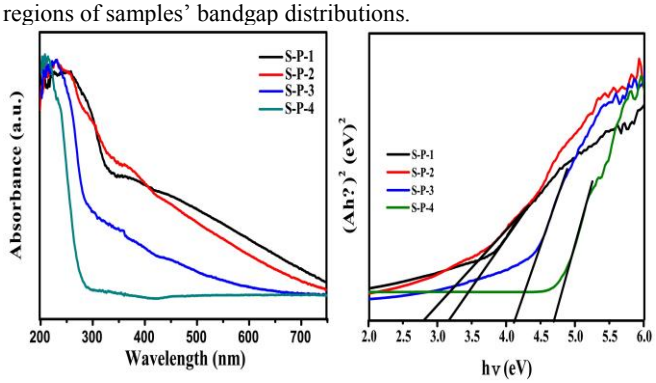

Figure 6. (a)UV-Vis DRS spectra of S-P-1, S-P-2, S-P-3 and S-P-4, (b) Band gap of S-P-1, S-P-2, S-P-3 and S-P-4

PL measurements were applied to determine the recombination behavior of electron-hole combinations after photoexcitation of the semiconductors at excitation at 220 nm[33]. The spectra are shown in Fig 7. Higher recombination of carriers yields lower separation efficiency of carriers. All of samples show similar peak at about 540nm. It is evident that the S-P-1, S-P-2, S-P-3 obviously emit less PL intensity than the S-P-4. This implies smaller recombination rates between the photocreated electrons and holes. Among these $SbPO_4$, the S-P-2 catalyst is the least luminescent. This is attributed to the possible excitonic behaviors of the moderately defective structures of semiconductors [34].

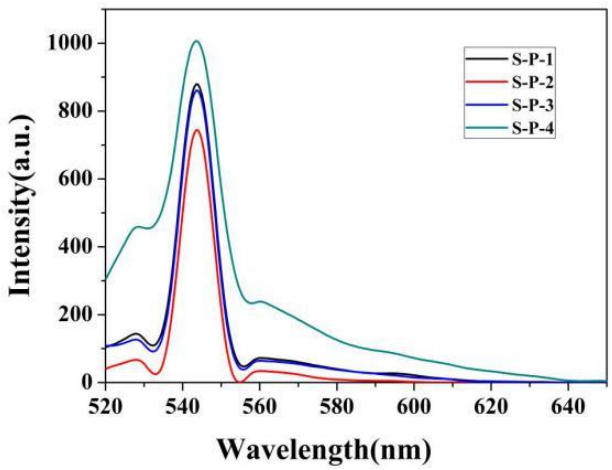

Figure 7.The PL spectra for S-P-1, S-P-2, S-P-3 and S-P-4 samples, respectively.

FTIR analysis

Figure 8 shows the FTIR spectra of S-P-1, S-P-2, S-P-3, S-P-4 and ILs. According to the literature,[32] the two vibrations centered at 1023 cm^{-1} and 953 cm^{-1} are due to the υ_1 symmetric vibrations, while the vibration around 1150 cm^{-1} can be associated with the corresponding υ_3 asymmetric stretching vibration of P-O bond. The vibration at 610 cm^{-1} corresponds to the bending vibration of O–P–O linkages. However, the vibration of the ILs evidently gives a different band shape (cyan line in the figure). This provides strong evidence for the absent of ILs in the as-prepared samples.

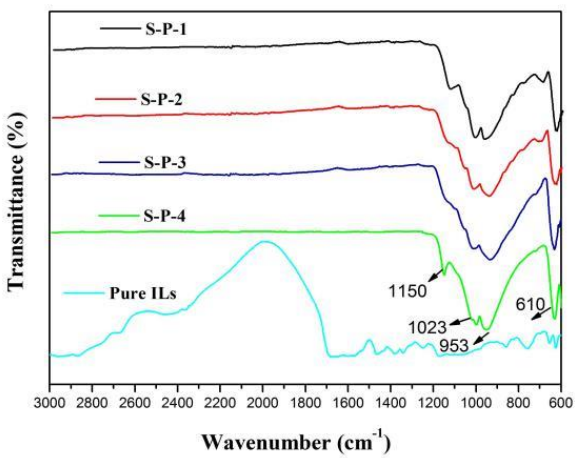

Figure 8.FTIR spectra of S-P-1, S-P-2, S-P-3, S-P-4 and ILs.

BET analysis

The nitrogen adsorption and desorption measurements for S-P-1, S-P-2, S-P-3 and S-P-4 are shown in Figure 9 and Table 2. From the results, the isotherm of S-P-1 and S-P-2 can be assigned to type IV with an indistinct hysteresis loop[35], which was attributed the mesoporous material. The isotherm of S-P-3 and S-P-4 presents II type isotherms, which demonstrates the absence of mesoporous material in the prepared samples[35]. The specific surface areas of S-P-1, S-P-2, S-P-3 and S-P-4 are 5.14, 6.98, 15.35 and 13.07 m^2/g, respectively. A slight increase in the specific surface area is observed when increasing the reaction temperature. This phenomenon maybe caused by thermal defragmentation of large particles. However, compared to the specific surface area of samples, the influence of specific surface area is negligible for the overall photocatalytic activity.

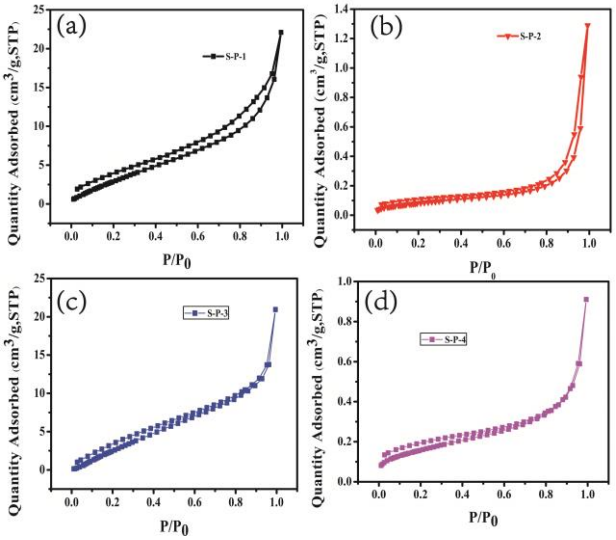

Figure 9. Adsorption-desorption isotherms of $SbP0_4$ prepared at different conditions.

Table 2. Structural parameters obtained from N_2 adsorption isotherms analysis.

Sample	S_{BET}(m^2g^{-1})	Pore volume(cm^3g^{-1})	Average pore size (nm)
S-P-1	5.14	0.032292	8.83273
S-P-2	6.98	0.044233	25.6388
S-P-3	15.35	0.029994	5.11134
S-P-4	13.07	0.029351	9.65675

Photocatalytic activity

Figure 10a and b show the time-course photocatalytic decolorations of RhB and MB over $SbPO_4$ prepared at different reaction temperature under UV light irradiation, along with the blank tests. Monitoring spectra of the photodegradation reaction of RhB and MB over S-P-2 are shown in the insets. From the figures, RhB and MB appear to be stable under UV light irradiation without the presence of $SbPO_4$. The degradation or adsorption of RhB and MB are negligible (about 3–7 % and 1-11 %) on the $SbPO_4$ without UV irradiation. Obviously, introductions of $SbPO_4$ can substantially improve the degradation rates of the dyes. The decoloration rate of RhB is about 86%, 99%, 97% and 73% over S-P-1, S-P-2, S-P-3 and S-P-4 after UV light irradiation for 45 min. Similarly, 79 %, 99 %, 91 % and 60 % MB was degraded over the samples after UV light irradiation for 60 min, respectively. All the removal efficiencies of the ionic-liquid-assisted $SbPO_4$ are better than these of 73% and 60% from the no-ionic-liquid-assisted $SbPO_4$.

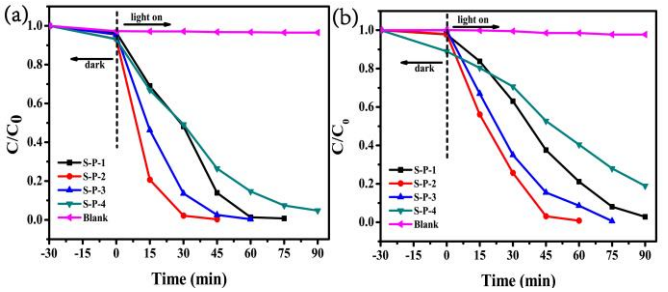

Figure 10. Photocatalytic degradation of RhB (a) and MB (b) by $SbPO_4$photocatalysts.

The kinetics of photocatalytic performance was also studied. The pseudo-first-order kinetic model reads

$$ln(C_0/C_t) = F(t) = kt$$

where k is the apparent reaction rate constant, C_0 and C_t are the initial concentration and the concentration at the reaction time of t. Natural logarithms of concentration ratios from the catalytic measurements were plotted as functions of reaction time in Figure 11a and b for the RhB and MB, respectively. The logarithmic data were fitted through the above formula, and the fitted lines were drawn in the same figures. The reaction rate constants of RhB over S-P-1, S-P-2, S-P-3, S-P-4 and without photocatalyst were calculated to 0.07161, 0.13304, 0.09496, 0.03464 and 0.00003 min^{-1}. These values were given in Figure 10a. With the increase of synthesis temperature, the rate constant of $SbPO_4$ samples first increased and then decreased. As shown in Figure 11b, the same results can also be observed by the degradation of MB. Thus, the ionic-liquid-assisted $SbPO_4$ microspheres exhibited higher photodegradation rate in the photocatalytic performance of RhB and MB. Especially, the S-P-2 possessed the largest rate constant during the whole period of 90 minutes of the UV irradiation. Such a value is 3.9 times of that of no-ionic-liquid-assisted $SbPO_4$ for the degradation of RhB.

The top degradation efficiency of S-P-2 over both RhB and MB was attributed to the flower-like microspherical morphology, high surface and narrow bandgap of the sample. The multiple reflections in microspheres leads to multi-reflection of the UV light, and trapping the photons in the samples. Compared to another two samples, S-P-2 possesses a larger contact area between the dyes and the synthetic crystal. This facilitates the catalytic reactions on the semiconductor surface. Additionally, the electronic structures also benefits its photocatalytic reactivity. Compared with $SbPO_4$ prepared at 140 ℃ or 180 ℃, the 160 ℃-fabricated microspheres has a narrower band gaps given by UV-Vis spectrum (Figure.6) but lower electron-hole recombination rate shown in the PL spectrum (Figure.7).All these three factors prompts S-P-2 as the best photocatalyst among the peers.

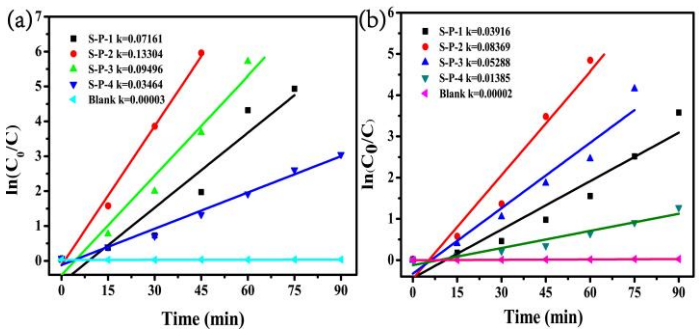

Figure 11. The pseudo-first-order kinetic model for the degradation of RhB (a) and MB (b) by $SbPO_4$photocatalysts.

We also tested the reusability of the $SbPO_4$ samples. Figure 12 shows the photocatalytic ability of RhB over $SbPO_4$ under UV light irradiation for five cycles. After 5 photocatalysis iterations, S-P-2 still kept significant photocatalytic robust with a degradation percentage of 94 %, confirming that the S-P-2 has good photostability under UV light.

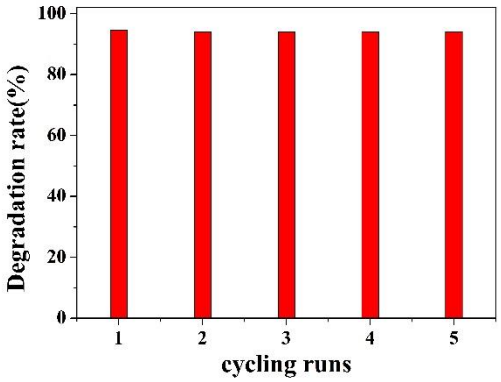

Figure 12. Cycling runs of S-P-2 for the photocatalytic degradation of RhB.

To understand the photocatalytic of $SbPO_4$, it is very important to detect main reactive species (such as h+, ·OH and O_2^- radicals) that are involved in the photocatalytic process. In the radical and hole trapping experiments, EDTA-Na_2 , isopropanol (IPA) and p-benzoquinone (BQ) were used as scavengers for h+, ·OH and O_2^- respectively. As shown in Figure 13, when no quenchers were added, the degradation efficiency of RhB was 99%. When IPA and $AgNO_3$ quencher were added, the RhB degradation efficiency was significantly reduced to 26% and 73%. When EDTA-Na_2 and p-benzoquinone (BQ) were added, the degradation efficiency of RhB decreased to 11% and 6%, respectively. These results indicate that O_2^- and h+ are the main active oxidizing species, and the order of affecting degradation efficiencies of RhB follows that of O_2^- > h+> ·OH >e^- similar to the results from other groups.

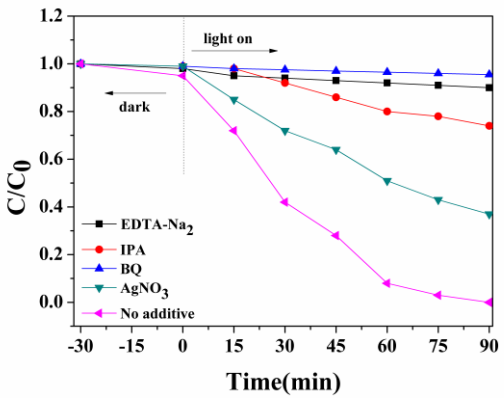

Figure 13. Effect of different quenchers on the RhB photodegradation by $SbPO_4$ under visible-light irradiation for 90 min.

The photocatalytic mechanism is proposed as follows. Under UV irradiation, the electrons originated from $SbPO_4$ which react with O_2 to form O_2^- radicals. O_2^- can further convert to ·OOH and ·OH. On the other hand, electrons could react with O_2 and H^+ to generate H_2O_2, which could also transform into ·OH. Moreover, the generated h^+ of $SbPO_4$ directly oxidizes RhB molecules rather than form ·OH to indirectly oxidize MB molecules. The photocatalytic process can thus be schematized as follows:

$$SbPO_4 + hv \rightarrow SbPO_4\ (e^- + h^+) \quad (1)$$

$$SbPO_4\ (e^-) + O_2 \rightarrow SbPO_4 + \cdot O_2^- \quad (2)$$

$$\cdot O_2^- + H_2O \rightarrow \cdot OOH + OH^- \quad (3)$$

$$e^- + O_2 + 2H^+ \rightarrow H_2O_2 \quad (4)$$

$$H_2O_2 + \cdot O_2 \rightarrow \cdot OH + OH^- + O_2 \quad (5)$$

$$MB/RhB + h^+ + \cdot OH + \cdot O2 \rightarrow \text{degradation products} \quad (6)$$

Conclusions

In summary, we have devised an hydrothermal synthesis to fabricate flower and sphere-like$SbPO_4$ with [BMIM][PO_4] as a coupling agent. The spherical shapes can be simply controlled through changing the hydrothermal reaction temperature. UV-Vis results shows that the bandgap of for S-P-1, S-P-2, S-P-3, S-P-4 was about 3.19, 2.80, 4.12 and 4.71 eV, respectively. The BET surface areas of the products have impact on the degradation of the as-synthesized samples. When used for the photocatalytic degradation of RhB and MB under UV light irradiation, the $SbPO_4$ prepared via ionic-liquid-assisted route demonstrate better photocatalytic effects than the no-ionic-liquid-assisted counterparts. From characterizations and scavenger tests, the high photocatalytic ability of $SbPO_4$ microspheres is attributed to the homogeneous spherical, relatively larger surface area and narrow band gap of the samples. The photocatalytic efficiency of RhB and MB comply with the following order S-P-2>S-P-3>S-P-1>S-P-4. Moreover, S-P-2 shows the highest degradation performance of both RhB and MB, considerably extending potential for research and practical applications.

Acknowledgments

The authors acknowledge with thanks the financial support of the National Natural Science Foundation of China (21601149) and Scientific Research Fund of Hunan Provincial Education Department, China (16B253), the Open Project Program of State Key Laboratory of Structural Chemistry, China (No. 20150018) and Hunan 2011 Collaborative Innovation Center of Chemical Engineering & Technology with Environmental Benignity and Effective Resource Utilization and the Oulu University Strategic Grant. T. Li acknowledges Oulu University Short-term International Research Visit grant during his stay in Finland.

Notes and references

[a] *College of Chemistry,Key Lab of Environment Friendly Chemistry and Application in Ministry of Education, Xiangtan University, Xiangtan, 411105, China.Fax: 86-731-8292251; Tel: 86-731-58292206; E-mail: fengli_xtu@hotmail.com; hnlth@xtu.edu.cn.*

[b] *Nano and Molecular Systems Research Unit, Faculty of Science, P. O. Box 3000, University of Oulu, FIN-90014, Finland*

(1) R. G. Chen, J. H. Bi, L. Wu, Z. H. Li,; X. Z. Fu,., *Crystal Growth & Design*, **2009,***9*, 1775-1779.
(2) S. Y. Wu, H. Zheng, Y. Y. Wu, W. Lin, T. Z. Xu, Guan, M., *Ceram Int*, **2014,** *40*, 14613-14620.
(3) X. Chen, D. X. Zhao, K. W. Liu, C. R. Wang, B.H. Li, Z.Z. Zhang, D. Z. Shen, , *ACS Appl Mater Inter*, **2015,***7*, 16070-16077.
(4) J. H. Sun, H. Yang, *Ceram Int*, **2014,** *40*, 6399-6404.
(5) X. Zhao, W. Q. Yao, Y. Wu, S. C. Zhang, H. P. Yang, Y. F. Zhu, , *J Solid State Chem*, **2006,***179*, 2562-2570.
(6) G. Q. Zhu, W. X Que, *J Clust Sci*, **2013,** *24*, 531-547.
(7) X. F. Zhang, L. L. Du, H. Wang, X. L. Dong, X. X. Zhang, C. Ma, H. C. Ma, *MicroporMesopor Mat* , **2013,***173*, 175-180.
(8) I. Paramasivam, J. M. Macak, T. Selvam, P. Schmuki, *ElectrochimActa*, **2008,** *54*, 643-648.
(9) X. Z. Liu, W. Si, C. Ding, S. L. Zang, *Chinese J InorgChem*, **2004,** *20*, 1445-1448.
(10) G. Alonzo, N. Bertazzi, P. Galli, G. Marci, M. A. Massucci, L. Palmisano, P. Patrono, F. Saiano, *Mater Res Bull*, **1998,***33*, 1233-1240.
(11) S. Y. Wu, H. Zheng, Y. W. Lian,; Y. Y. Wu , *Mater Res Bull* , **2013,***48*, 2901-2907.
(12) X. R. Yan, T. Bai, M. L. Huo, Y. P. Zhang, X. Y. Guo, *Chinese J Catal*, **2004,***25*, 120-124.
(13) Y. Huang, G. Xie, S. Chen, S. Gao, *J Solid State Chem*, **2011,** *184*, 502-508.
(14) X. Lin, F. Huang, W. Wang, Y. Wang, Y. Xia, J. Shi, *ApplCatal A: Gen*, **2006,***313*, 218-223.
(15) M. Ahlawat, G. V. Vazquez, M. Nalin, Y. Messaddeq, S. Ribeiro, R. Kashyap, *J Non-Cryst Solids*, **2010,** *356*, 2360-2362.
(16) Q. Han, L. Chen, M. Wang, X. Yang, L. Lu, X. Wang , *Mat SciEng B*, **2010,** *166*, 118-121.
(17) S. P. Hu, C.Y Xu. F. X. Ma, L. Cao, L. Zhen, *Dalton T*, **2014,** *43*, 8439-8445.
(18) D.N Liu, G. H. He, L. Zhu, W.Y. Zhou, Y.H. Xu, *Appl Surf Sci*, **2012,***258*, 8055-8060.
(19) Y. Wang, L. li, G. Li, *RSC Adv*, **2012,** *2*, 12999-13006.
(20) J. B. Biswal, S. S. Garje, N. Revaprasadu, *Polyhedron*, **2014,** *80*, 216-222.
(21) L. Qi, *CoordinChem Rev*, **2010,***254*, 1054-1071.
(22) K. S. Yao, W. W. Lu, J. J. Wang, *Mater ChemPhys*, **2011,** *130*, 1175-1181.
(23) Y. Z. Wu, X. P. Hao, J. X. Yang, F. Tian, M. H. Jiang, , *Mater Lett*, **2006,***60*, 2764-2766.
(24) S. L. Yu, B. C. Liu, Q. Wang, Y. X. Gao, Y. Shi, X. Feng, X. T. An, L. X. Liu, J. Zhang, *ACS Appl Mater Inter*, **2014,***6*, 10283-10295.
(25) T. Sivakumar Natarajan, H. C. Bajaj, R. J. Tayade, , *Crystengcomm* ,**2015,** *17*, 1037-1049.
(26) H. Zhang, Q. Zhu, Y. Zhang, Y. Wang, L. Zhao, B. Yu, *Adv Funct Mater*, **2007,***17*, 2766-2771.
(27) V. Sudarsan, K. P. Muthe, J. C. Vyas, S. K. Kulshreshtha, *J Alloy Compd*, **2002,***336*, 119-123.
(28) Y. N. Guo, X. Yang, F. Y. Ma, K. X. Li, L. Xu, X. Yuan, Y. H. Guo , *Appl Surf Sci*, **2010,***256*, 2215-2222.
(29) B. Pan, Y. Wang, Y. Y. Liang, S. J. Luo, W. Y. Su, X. X. Wang , *Int J Hydrogen Energ*, **2014,***39*, 13527-13533.
(30) C. S. Pan, Y. F. Zhu, *J Mater Chem*, **2011,** *21*, 4235-4241.
(31) S. Vyas, C .Dreyer, J. Slingsby, et al. Journal of Physical Chemistry A, **2014**, 118(34):6873.
(32) G. H. Liu, S. W .Liu, Q. F. Lu, H. Y. Sun, Z. L. Xiu, *IndEngChem Res*, **2014,***53*, 13023−13029.
(33) B.S. Naidu, V. Sudarsan, R. K. Vatsa, Journal of Nanoscience & Nanotechnology, **2009**, 9(5):2997.
(34) C. Yang, L. Zhang, Z. Wang, et al. Materials Science & Engineering B, **2016**, 207:39-46.
(35) M. Kruk, M. Jaroniec, *Chem Mate*, *r***2001,** *13*, 3169-3183.